Mid-altitude wind measurements with mobile Rayleigh Doppler lidar incorporating system-level optical frequency control method

Haiyun Xia,* Xiankang Dou, Dongsong Sun, Zhifeng Shu, Xianghui Xue, Yan Han, Dongdong Hu, Yuli Han, and Tingdi Cheng

Laser Remote Sensing Laboratory, School of Earth and Space Sciences, University of Science and Technology of China, 96 Jinzhai Road, Hefei, Anhui, 230026, China

hsia@ustc.edu.cn

Abstract: A mobile Rayleigh Doppler lidar based on double-edge technique is developed for mid-altitude wind observation. To reduce the systematic error, a system-level optical frequency control method is proposed and demonstrated. The emission of the seed laser at 1064 nm is used to synchronize the FPI in the optical frequency domain. A servo loop stabilizing the frequency of the seed laser is formed by measuring the absolute frequency of the second harmonic against an iodine absorption line. And, the third harmonic is used for Rayleigh lidar detection. The frequency stability is 1.6 MHz at 1064 nm over 2 minutes. A locking accuracy of 0.3 MHz at 1064 nm is realized. In comparison experiments, wind profiles from the lidar, radiosonde and European Center for Medium range Weather Forecast (ECMWF) analysis show good agreement from 8 km to 25 km. Wind observation over two months is carried out in Urumqi ($42.1°N$, $87.1°E$), northwest of China, demonstrating the stability and robustness of the system. For the first time, quasi-zero wind layer and dynamic evolution of high-altitude tropospheric jet are observed based on Rayleigh Doppler lidar in Asia.

OCIS codes: (010.0010) Atmospheric and oceanic optics; (120.0280) Remote sensing and sensors; (280.3340) Laser Doppler velocimetry; (280.3640) Lidar.

References and links

1. A. Stoffelen, J. Pailleux, E. Källen, J. M. Vaughan, L. Isaksen, P. Flamant, W. Wergen, E. Andersson, H. Schyberg, A. Culoma, R. Meynart, M. Endemann, and P. Ingmann, "The atmospheric dynamics mission for global wind field measurement," Bull. Am. Meteorol. Soc. **86**(1), 73–87 (2005).
2. P. Hays, M. Dehring, L. Fisk, P. Tchoryk, I. Dors, J. Ryan, J. Wang, M. Hardesty, B. Gentry, and F. Hovis, "Space-based Doppler winds lidar: a vital national need," In response to national research council (NRC) decadal study request for information (RFI), May (2005).
3. European Space Agency ESA, *ADM-Aeolus science report: ESA SP-1311* (ESA Communication Production Office, 2008).
4. R. M. Huffaker and R. M. Hardesty, "Remote sensing of atmospheric wind velocities using solid-state and CO_2 coherent laser systems," Proc. IEEE **84**(2), 181–204 (1996).
5. H. Xia, D. Sun, Y. Yang, F. Shen, J. Dong, and T. Kobayashi, "Fabry-Perot interferometer based Mie Doppler lidar for low tropospheric wind observation," Appl. Opt. **46**(29), 7120–7131 (2007).
6. C. L. Korb, B. M. Gentry, S. X. Li, and C. Flesia, "Theory of the double-edge technique for Doppler lidar wind measurement," Appl. Opt. **37**(15), 3097–3104 (1998).
7. C. Flesia and C. L. Korb, "Theory of the double-edge molecular technique for Doppler lidar wind measurement," Appl. Opt. **38**(3), 432–440 (1999).
8. Z. S. Liu, D. Wu, J. T. Liu, K. L. Zhang, W. B. Chen, X. Q. Song, J. W. Hair, and C. Y. She, "Low-altitude atmospheric wind measurement from the combined Mie and Rayleigh backscattering by Doppler lidar with an iodine filter," Appl. Opt. **41**(33), 7079–7086 (2002).
9. J. A. McKay, "Assessment of a multibeam Fizeau wedge interferometer for Doppler wind lidar," Appl. Opt. **41**(9), 1760–1767 (2002).
10. D. Bruneau, A. Garnier, A. Hertzog, and J. Porteneuve, "Wind-velocity lidar measurements by use of a Mach-Zehnder interferometer, comparison with a Fabry-Perot interferometer," Appl. Opt. **43**(1), 173–182 (2004).

#167584 - $15.00 USD Received 27 Apr 2012; revised 27 May 2012; accepted 30 May 2012; published 22 Jun 2012

11. N. Cézard, A. Dolfi-Bouteyre, J. P. Huignard, and P. H. Flamant, "Performance evaluation of a dual fringe-imaging Michelson interferometer for air parameter measurements with a 355 nm Rayleigh-Mie lidar," Appl. Opt. **48**(12), 2321–2332 (2009).
12. O. Reitebuch, C. Lemmerz, E. Nagel, U. Paffrath, Y. Durand, M. Endemann, F. Fabre, and M. Chaloupy, "The airborne demonstrator for the direct-detection Doppler wind lidar ALADIN on ADM-Aeolus. Part I: Instrument design and comparison to satellite instrument," J. Atmos. Ocean. Technol. **26**(12), 2501–2515 (2009).
13. U. Paffrath, C. Lemmerz, O. Reitebuch, B. Witschas, I. Nikolaus, and V. Freudenthaler, "The airborne demonstrator for the direct-detection Doppler wind lidar ALADIN on ADM-Aeolus. Part II: Simulations and Rayleigh Receiver Radiometric performance," J. Atmos. Ocean. Technol. **26**(12), 2516–2530 (2009).
14. M. L. Chanin, A. Garnier, A. Hauchecorne, and J. Porteneuve, "A Doppler lidar for measuring winds in the middle atmosphere," Geophys. Res. Lett. **16**(11), 1273–1276 (1989).
15. A. Garnier and M. L. Chanin, "Description of a Doppler Rayleigh LIDAR for measuring winds in the middle atmosphere," Appl. Phys. B **55**(1), 35–40 (1992).
16. C. Souprayen, A. Garnier, A. Hertzog, A. Hauchecorne, and J. Porteneuve, "Rayleigh-Mie Doppler wind lidar for atmospheric measurements. I. Instrumental setup, validation, and first climatological results," Appl. Opt. **38**(12), 2410–2421 (1999).
17. C. Souprayen, A. Garnier, and A. Hertzog, "Rayleigh-Mie Doppler wind lidar for atmospheric measurements. II. Mie scattering effect, theory, and calibration," Appl. Opt. **38**(12), 2422–2431 (1999).
18. C. A. Tepley, "Neutral winds of the middle atmosphere observed at Arecibo using a Doppler Rayleigh lidar," J. Geophys. Res. **99**(D12), 25781–25790 (1994).
19. J. S. Friedman, C. A. Tepley, P. A. Castleberg, and H. Roe, "Middle-atmospheric Doppler lidar using an iodine-vapor edge filter," Opt. Lett. **22**(21), 1648–1650 (1997).
20. D. Rees, M. Vyssogorets, N. P. Meredith, E. Griffin, and Y. Chaxell, "The Doppler wind and temperature system of the ALOMAR lidar facility: overview and initial results," J. Atmos. Sol. Terr. Phys. **58**(16), 1827–1842 (1996).
21. U. von Zahn, G. von Cossart, J. Fiedler, K. H. Fricke, G. Nelke, G. Baumgarten, D. Rees, A. Hauchecorne, and K. Adolfsen, "The ALOMAR Rayleigh/Mie/Raman lidar: Objectives, configuration, and performance," Ann. Geophys. **18**, 815–833 (2000).
22. G. Baumgarten, "Doppler Rayleigh Mie Raman lidar for wind and temperature measurements in the middle atmosphere up to 80 km," Atmos. Meas. Tech. Discuss. **3**(6), 1509–1518 (2010).
23. W. Huang, X. Chu, J. Wiig, B. Tan, C. Yamashita, T. Yuan, J. Yue, S. D. Harrell, C.-Y. She, B. P. Williams, J. S. Friedman, and R. M. Hardesty, "Field demonstration of simultaneous wind and temperature measurements from 5 to 50 km with a Na double-edge magneto-optic filter in a multi-frequency Doppler lidar," Opt. Lett. **34**(10), 1552–1554 (2009).
24. B. M. Gentry, H. Chen, and S. X. Li, "Wind measurements with 355-nm molecular Doppler lidar," Opt. Lett. **25**(17), 1231–1233 (2000).
25. F. Shen, H. Hyunki Cha, J. Dong, D. Kim, D. Sun, and S. O. Kwon, "Design and performance simulation of a molecular Doppler wind lidar," Chin. Opt. Lett. **7**(7), 593–597 (2009).
26. T. Schröder, C. Lemmerz, O. Reitebuch, M. Wirth, C. Wührer, and R. Treichel, "Frequency jitter and spectral width of an injection-seeded Q-switched Nd:YAG laser for a Doppler wind lidar," Appl. Phys. B **87**(3), 437–444 (2007).
27. K. Nicklaus, V. Morasch, M. Hoefer, J. Luttmann, M. Vierkötter, M. Ostermeyer, J. Höffner, C. Lemmerz, and D. Hoffmann, "Frequency stabilization of Q-switched Nd:YAG oscillators for airborne and spaceborne lidar systems," Proc. SPIE **6451**, 1–12 (2007).
28. F. E. Hovis, M. Rhoades, R. L. Burnham, J. D. Force, T. Schum, B. M. Gentry, H. Chen, S. X. Li, J. W. Hair, A. L. Cook, and C. A. Hostetler, "Single-frequency lasers for remote sensing," Proc. SPIE **5332**, 263–270 (2004).
29. H. Xia and J. Yao, "Characterization of sub-picosecond pulses based on temporal interferometry with real-time tracking of higher-order dispersion and optical time delay," J. Lightwave Technol. **27**(22), 5029–5037 (2009).
30. M. S. Fee, K. Danzmann, and S. Chu, "Optical heterodyne measurement of pulsed lasers: Toward high-precision pulsed spectroscopy," Phys. Rev. A **45**(7), 4911–4924 (1992).
31. M. Wirth, A. Fix, P. Mahnke, H. Schwarzer, F. Schrandt, and G. Ehret, "The airborne multi-wavelength water vapor differential absorption lidar WALES: system design and performance," Appl. Phys. B **96**(1), 201–213 (2009).
32. L. A. Rahn, "Feedback stabilization of an injection-seeded Nd: YAG laser," Appl. Opt. **24**(7), 940–942 (1985).
33. F. T. S. Yu and S. Yin, *Fiber Optic Sensors* (Marcel Dekker, Inc., New York, 2002), Chap. 5.3.1.
34. A. T. Young and G. W. Kattawar, "Rayleigh-scattering line profiles," Appl. Opt. **22**(23), 3668–3670 (1983).
35. A. Dabas, M. Denneulin, P. Flamant, C. Loth, A. Garnier, and A. Dolfi-Bouteyre, "Correcting winds measured with a Rayleigh Doppler lidar from pressure and temperature effects," Tellus A **60**(2), 206–215 (2008).
36. M. Weissmann and C. Cardinali, "Impact of airborne Doppler lidar observations on ECMWF forecasts," Q. J. R. Meteorol. Soc. **133**(622), 107–116 (2007).
37. M. Weissmann, R. H. Langland, P. M. Pauley, S. Rahm, and C. Cardinali, "Influence of airborne Doppler wind lidar profiles near Typhoon Sinlaku on ECMWF and NOGAPS forecasts," Q. J. R. Meteorol. Soc. **138**, 118–130 (2011).
38. K. Mohanakumar, *Stratosphere Troposphere Interactions: An Introduction* (Springer Science, 2008), Chap.1.
39. H. Xia and C. Zhang, "Ultrafast ranging lidar based on real-time Fourier transformation," Opt. Lett. **34**(14), 2108–2110 (2009).
40. H. Xia and C. Zhang, "Ultrafast and Doppler-free femtosecond optical ranging based on dispersive frequency-

#167584 - $15.00 USD Received 27 Apr 2012; revised 27 May 2012; accepted 30 May 2012; published 22 Jun 2012

1. Introduction

Global Wind field measurement throughout the troposphere and lower stratosphere are essential for understanding and predicting the future state of the earth-atmosphere system. High accuracy and real-time wind measurement will also address some vital needs such as Air Force operations, hurricane tracking, epidemic prevention and potential chemical-biological release trajectory prediction. Although current wind data are obtained widely from surface stations, buoys, ships, radiosonde networks, aircraft along flight paths, ground-based wind profilers, radiometer and space-borne scatterometer, cloud or water vapor tracking satellites, there are still some problems, such as the inadequate coverage and the low temporal or spatial resolutions. The space-borne Doppler Wind Lidar (DWL) is now regards as the potential way to fill the global wind data requirements and gaps limited by the mentioned methods above [1–3]. On the one hand, the Doppler shift can be retrieved from the spectrally narrowband Mie backscattering using coherent wind lidar by optically beating the atmosphere echo with a local continuous-wave oscillator laser [4]. On the other hand, the Doppler shift carried by Mie or Rayleigh backscattering can be determined directly using high-resolution frequency discriminators, such as Fabry-Perot Interferometer (FPI) [5–7], iodine absorption filter [8], Fizzeau interferometer [9], Mach-Zehnder interferometer [10] and Michelson interferometer [11]. In the ADM-Aeolus (Atmospheric Dynamic Mission Aeolus) payload Atmospheric Laser Doppler Instrument (ALADIN), a Fizzeau interferometer and a double-edge FPI are used to analyze the Mie and Rayleigh backscattering, respectively [12,13].

In the altitude range from upper troposphere to the stratosphere, where the Mie backscattering signal is usually weak, Doppler Rayleigh lidar is the unique wind remote sensing instrument with high spatial and temporal resolution. Although the first direct-detection Doppler lidar has been demonstrated about forty years ago, there are only few reports of stratospheric wind measurements using direct-detection Doppler Rayleigh lidars. The wind detection up to 50km was first realized using a double-edge FPI as the frequency discriminator at the Observatory of Haute Provence (OHP), France [14–17]. A similar Rayleigh lidar based on single FPI was developed for wind measurement to an altitude near 60km at Arecibo Observatory [18]. Later, the pressure-scanned FPI was replaced by a molecular iodine filter [19]. Both FPI and iodine filter were reported for mid-altitude wind measurement at the ALOMAR research station near Andenes, Norway [20–22]. Recent experiments demonstrated its ability of measuring the wind and temperature up to 80km.

The working wavelength of all literatures cited in the last paragraph is at 532 nm. Recently, simultaneous wind and temperature measurements with a sodium filter at 589 nm were reported from 10 km to 45 km at Fort Collins, Colorado [23]. Taking advantage of the λ^{-4} dependence of the Rayleigh backscattering, the GLOW (Goddard Lidar Observatory for Winds) mobile Doppler lidar was developed using double-edge FPI and frequency-tripled Nd:YAG laser at 355 nm at NASA Goddard space flight center [24]. A similar mobile Rayleigh Doppler wind lidar was built at the University of Science and Technology of China (USTC) [25].

2. Instrument and method

The principle of double-edge technique used in Rayleigh Doppler wind lidar has been described in detail by several groups [7, 13, 16, 25]. It is reviewed briefly here, as illustrated in Fig. 1. The capacitively stabilized and piezo-electrically tunable FPI used in this work contains three channels. The frequency of the laser is locked at the crosspoint of the double-edge channels by scanning the cavity length of the FPI, where the piezoelectric transducers is driven by a feedback signal in proportion to the transmission of the outgoing laser on the locking channel. Wind detection is implemented by measuring the transmission changes of the backscattering on the double-edge channels due to the Doppler shift, represented by the area changes of the shades in Fig. 1.

#167584 - $15.00 USD Received 27 Apr 2012; revised 27 May 2012; accepted 30 May 2012; published 22 Jun 2012

We focus on techniques reducing systematic errors in this paper. In the development of direct detection Doppler lidars, one of the most challenging goals is the frequency stability control of the system. A wind velocity of 1 m/s equates to a frequency Doppler shift of 5.63 MHz at the working wavelength of 355 nm. Transferred to the fundamental wavelength of the pulse laser, a frequency stability of 1.88 MHz at 1064 nm should be guaranteed. Various methods have been demonstrated to improve the frequency stability of a Q-switched Nd:YAG oscillator in a Doppler lidar system, such as pulse-build-up method, cavity dither method, modified Pound-Drever-Hall method and ramp-fire method [26, 27]. Comparisons of these methods came to a conclusion that the ramp-fire method offers the highest frequency stability and therefore be adopted in the ALADIN airborne demonstrator [12, 27] and the GLOW system [28].

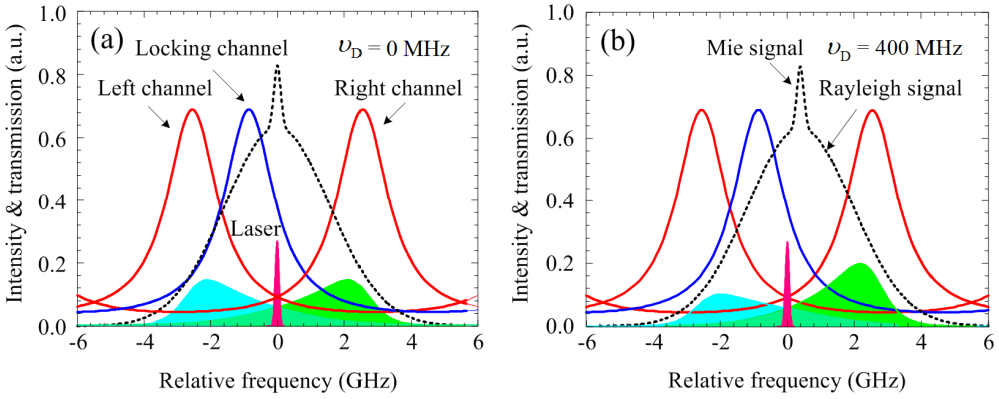

Fig. 1. Principle of the double-edge technique adopted in the Rayleigh Doppler wind lidar. The spectrum of backscattering is assumed to be the superimposition of Mie and Rayleigh spectrums. The impact of Brillouin backscattering is not considered in this figure. (a) Without Doppler shift ($\upsilon_D = 0\,MHz$). (b) With Doppler shift ($\upsilon_D = 400\,MHz$). υ_D is the Doppler shift carried on the atmosphere backscattering.

The USTC Rayleigh Doppler lidar uses a commercial available flash-pumped and frequency-tripled Nd:YAG laser (Continuum Model Powerlite 9030), where the frequency stabilization is realized by minimizing the Q-switch build-up time. To enhance the performance of the lidar, a system-level optical frequency control scheme is proposed and demonstrated. Schematic diagram of the Rayleigh Doppler lidar is shown in Fig. 2. The transmitter is comprised of four function modules: the continuous wave (CW) seed laser, the power laser, an absolute frequency control module based on iodine cell and a heterodyne unit for pulse-to-pulse frequency jitter monitoring. The frequency-tripled Nd:YAG power laser adopts a MOPA (injection-seeded master oscillator power amplifier) configuration, which emits 355 nm laser with pulse energy about 350 mJ at a repetition rate of 30 Hz. After compressing the beam divergence through an expander, the outgoing laser beam is directed to a reflecting mirror on the top of the Schmidt-Cassegrain telescope (450 mm diameter) and pointed to the atmosphere coaxially with the line-of-sight (LOS) of the telescope. A matching azimuth-over-elevation scanner permits full sky perspective. The atmosphere backscattering is focused into a UV optical fiber (200 μm), which transfers the signal from the telescope to the optical receiver. At the other end of the multimode fiber, the light is collimated and split into three beams: one for energy monitoring and the other two beams passing through an FPI parallelly for Doppler shift measurement. In the new developed three-channel FPI, two channels are used as the implementation of the double-edge technique at 355 nm, while the third channel illuminated by CW from the seed laser is used for frequency-locking. The system parameters are summarized in Table 1.

#167584 - $15.00 USD Received 27 Apr 2012; revised 27 May 2012; accepted 30 May 2012; published 22 Jun 2012

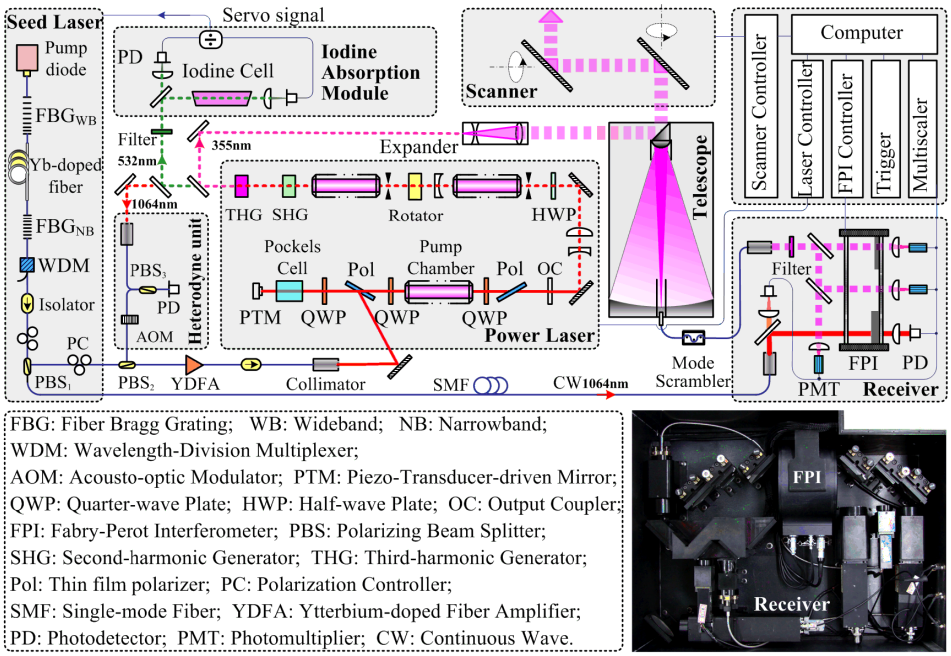

Fig. 2. Schematic diagram of the Rayleigh Doppler Lidar with system-level optical frequency control, and interior view of the compact receiver (inset, lower right corner).

Table.1 Key parameters of the mobile Rayleigh Doppler Lidar

Parameter	Value
Transmitter	
Wavelength (nm)	355
Laser 1/e width (MHz)	200
Laser energy/pulse (mJ)	350
Laser repetition rate (Hz)	30
Transceiver	
Telescope aperture (mm)	45
Field of view (mrad)	0.2
Scan range (°)	360°×90°
Zenith angle (°)	30°
Optical efficiency (%)	85
Receiver	
Etalon FSR (GHz)	12
FWHM of edge channels (GHz)	1.7
Edge channel separation (GHz)	5.1
FWHM of locking channel (GHz)	0.2
Locking separation (GHz)	2.45
Etalon peak transmission (%)	60
PMT Quantum Efficiency (%)	21

Some optical setup modifications and the unique system-level optical control method adopted make our system quite different from the ALADIN and GLOW systems. In the ALADIN instrument [3], the Rayleigh FPI is evacuated between the reflecting plates and manufactured with fixed cavity by optically contacting the plates to a fused silica spacer. In the instrument initialization, the seed laser should be frequency tunable over a spectral range of 11GHz to calibrate the spectral response of the FPI. The frequency holding and tuning of the seed laser is realized by defining a different frequency from another stable reference laser operating at a quasi fixed-frequency [26]. The frequency tuning range (12 GHz) is far beyond the free spectral range of the low power oscillator (FSR = 250 MHz) in this work, making the

#167584 - $15.00 USD Received 27 Apr 2012; revised 27 May 2012; accepted 30 May 2012; published 22 Jun 2012

calibration procedure at risk of contamination of the second longitudinal mode arising from the low power oscillator. In contrast to the ALADIN system, we use a cavity tunable FPI as in the GLOW system. The characterization of the FPI transmission is realized in a fast way by scanning the spacing between the plates via piezoelectric transducers, while the laser is kept at fixed frequency. Based on a single close-loop servo system incorporated in the FPI controller, long-term relative frequency drift between the laser pulses and the FPI is eliminated in laboratory [5]. In the previous version of our Rayleigh lidar [25], the close-loop servo system is based on the transmission of the 355 nm laser pulse going through the locking channel, which has a FWHM of 1.7 GHz. In this work, the reflecting plates of the FPI (ICOS model CS100) are updated. Specifically, the working wavelength of locking channel is changed from 355 nm to 1064 nm with a narrower FWHM (full width at half maximum) of 230 MHz, improving the locking sensitivity since the slope of later locking channel becomes much steeper. Furthermore, the measurement of the relative frequency between the outgoing laser and the FPI shows higher SNR (signal-to-noise ratio) when the illumination is changed from pulsed mode to continuous mode.

The following challenges we encountered in the development of the lidar improve its performance finally. Firstly, in the former version, the servo signal feed back to the piezoelectric transducers in the FPI is proportional to the transmission of the laser pulse on the locking channel, where the transmission function is the convolution of the instrument response function and the unit-area normalized spectrum of the pulse. Usually, the frequency locking accuracy is worse than the amplitude of frequency jitter, as the out-of-step operation of the servo system cannot predict the random pulse-to-pulse frequency jitter and linewidth fluctuation arising in the MOPA process. For the purpose of high SNR in mid-altitude wind measurements, integration time of half an hour or even longer is used for ground-base Doppler lidar systems. During such a long period, a poor locking accuracy will degrade the detection sensitivity of the double-edge technique. Secondly, if a fast cavity length scanning is performed, the FPI cannot respond instantaneously, and electronic noise will make the plates vibrating about their mean position with small random amplitude. The RMS deviations of the cavity length is 230 pm/90 pm according to response time of 0.2 ms/2 ms, which broadens the transmission curve of the order of 1.6 MHz/0.6 MHz effectively at 355 nm. For system stability, slow scanning of the FPI is preferred based on CW locking mode. Thirdly, the optical layout of the receiver is simpler and more compact than the GLOW system, providing easier optical alignment and stable performance. And, optical interference between the FPI channels is easier to eliminate, as the locking channel works at a different wavelength. Furthermore, a locking channel with smaller aperture is needed, since the CW laser is collimated from a single-mode fiber with core diameter of 9 μm instead of from a 200 μm multimode fiber.

Different from the ALOMAR [21] system and Liu's system [8], the fiber seed laser used in this work generates only single-frequency output at 1064 nm (Continuum Model SI2000). Fiber coupling of the seed laser allows its separation from the pulsed oscillator and place in a temperature-controlled chamber. In the seed laser, a cavity is established by two fiber Bragg gratings (FBG) that are fusion spliced to a piece of Ytterbium-doped fiber. The laser is excited through the high-reflecting wideband FBG_{WB} using the output of a single mode pump diode, while the narrowband FBG_{NB} serves as an output coupler. Temperature control of the FBG_{NB} and FBG_{WB} provides wavelength tuning coefficients of 1.5 GHz/K and 0.3 GHz/K, respectively. In order to suppress the possible second longitudinal mode efficiently, an Ytterbium-doped fiber amplifier is used to amplify the power of the seed laser to an order of 100 mW to saturate the gain of the pulsed oscillator.

To further improve the system stability and achieve semi-automatic system operation, we measure the absolute frequency of the second harmonic of the seed laser against the steep absorption line 1109 of iodine. A servo loop controlling the frequency of seed laser is formed by guiding the residual 532 nm pulse train through the absorption cell and measuring the power ratio before and after it. In this scheme, the actural frequency fluctuation results mainly

#167584 - $15.00 USD Received 27 Apr 2012; revised 27 May 2012; accepted 30 May 2012; published 22 Jun 2012

from two aspects: the frequency drift of the seed laser and the frequency dithering produced during the process of matching the cavity of the low power oscillator to the seed laser frequency. To differentiate the effects from each other, we characterize the frequency stability of the oscillator firstly, following a heterodyne method. Detailed close-loop control of the seed laser and characterization of the system stabilization will be introduced in the following section.

3. Characterization of the system stabilization

In the recent development of Rayleigh Doppler lidars, great efforts have been dedicated to system stabilization and calibration. Heterodyne detection has been one of the most popular methods for studying the pulse-to-pulse fluctuations in laser parameters, such as frequency stability, pulse width and intensity [26, 29–31]. The measurement accuracy of instantaneous frequency of laser pulses based on heterodyne method has been investigated theoretically and experimentally [30]. In a recent implementation [31], the authors declared that the pulse-to-pulse frequency jitter was measured be to better than 300 kHz RMS (root-mean-square) using heterodyne technique. Where, the passively Q-switched Nd:YAG oscillator produces laser pulses with FWHM of about 8 ns.

In this experiment, the all-fiber configuration of the heterodyne module shows superiority of simple optical alignment and easy detection. A conjunction of in-line fiber polarizing beam splitter (PBS) and polarization controller (PC) allows arbitrary power splitting ratio and perfect linear polarization of the CW in our system. A small fraction of the seed laser is coupled out and frequency shifted by 400 MHz using an acousto-optic modulator, as shown in Fig. 2. Beat notes of a laser pulse with the fundamental CW is generated on a 3.5 GHz-bandwidth InGaAs PIN photodetector (PD). The output of the PD (microwave pulse train) is sampled by a high-speed digitizer with analog bandwidth of 2 GHz (Agilent U1062A). Its power spectrum is calculated using fast Fourier transform (FFT). Figure 3(a) shows a typical heterodyne signal and its FFT spectrum. From the power spectrum, the frequency offset of each output pulse relative to the seed laser is calculated as the deviation of the spectral centroid from the frequency shift introduced by the AOM. Figure 3(b) shows a short-term tracking of the frequency center of pulse train and its corresponding histogram distribution. The frequency stability is 1.6 MHz RMS over 2 minutes. The frequency offset between the power laser and the seed laser is 6.8 MHz.

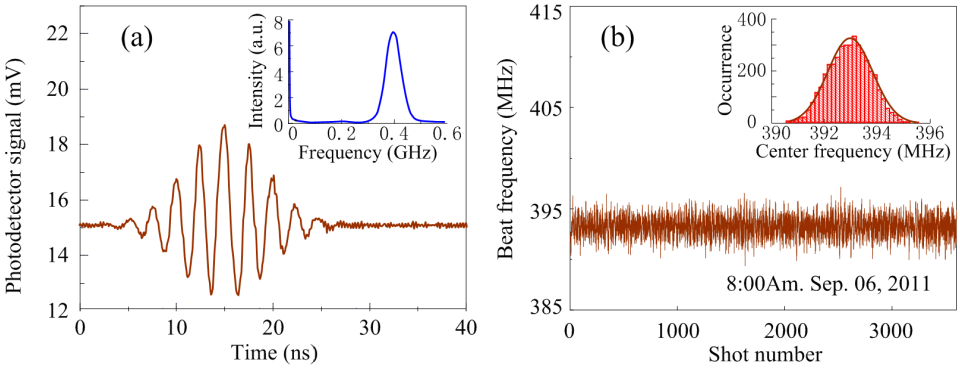

Fig. 3. Frequency stability of the seed laser. (a) A heterodyne signal and its FFT spectrum (inset, upper right corner). (b) Frequency centroid measured over 2 minutes and its histogram distribution (inset, upper right corner).

The frequency offset between the power laser and the seed laser depends mainly on the stable single-mode operation of the low power oscillator. This is achieved by injection of seed laser with Q-switch build-up time minimization technique, where the cavity length of the low power oscillator is dithered by a small fraction of one FSR (250 MHz) about the resonance position. In this scheme, the oscillator works at a cavity length either slightly shorter or

#167584 - $15.00 USD Received 27 Apr 2012; revised 27 May 2012; accepted 30 May 2012; published 22 Jun 2012

slightly longer than the average cavity length, making the output frequency of the oscillator alternates between two succeeding shots. Considering this fact, the amplifier stages operate at half of the oscillator repetition rate to select the odd pulses only [32]. The dither amplitude for achieving long term single frequency operation is about 2% of the FSR in this work. Furthermore, it has been recognized that the nonlinear process may result in displaced or distorted spectrum of the laser pulses [30].

We set the minimum integration time to 2 minutes for two reasons. Firstly, wind profiles with short temporal resolution are required for the studies of gravity wave in the troposphere. Secondly, the frequency stability and frequency offset between the power laser and the seed laser is analyzed in every 2 minutes statistically. Before accumulating the 15 raw data over half an hour for wind measurement in the mid-altitude, a quality check is carried out for each raw data with criteria that the frequency stability should be within ± 1.88 MHz and the drift of the frequency offset should be within ± 1 MHz.

In this work, the absolute frequency of the seed laser is stabilized against an iodine cell. And the relative frequency drift between the seed laser and the FPI is eliminated based on the single close-loop servo system incorporated in the FPI controller. Thus, the long-term system stability is dominated by the possible frequency drift of the low power oscillator caused by its cavity change due to the temperature fluctuation of the cooling water.

The calibration process of the Rayleigh lidar is almost the same as we did in the Mie lidar [5]. The FSR of an evacuated FPI is determined by its cavity length l only, i.e., $FSR = c / 2l$, where, c is the speed of light in vacuum. Thus, the locking channel working at 1064 nm and the double-edge channels at 355 nm can be fabricated on a pair of optical plates with identical FSR. Characterization of the FPI transmission curves is performed by scanning its cavity length. A capacitance bridge fabricated on the mirror plates is used to sense changes in parallelism and cavity spacing. Three piezoelectric actuators are used to turn the cavity spacing and permit elimination of parallelism errors.

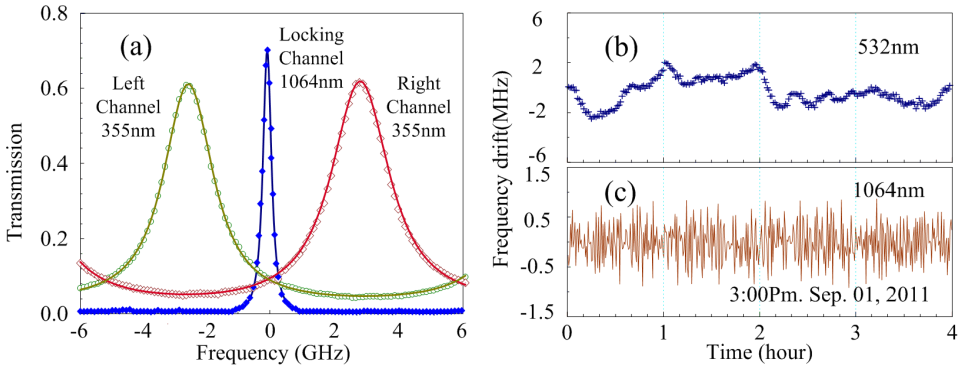

Fig. 4. (a) Measured transmission curves of the FPI. Solid lines are the Gaussian fit results. (b) Residual frequency drift of 532 nm pulse train. (c) Frequency locking accuracy of the FPI to the seed laser.

Figure 4(a) shows the measured results. Then the raw data are fitted to a transmission function, which will be introduced as Eq. (3) in the wind retrieval algorithm next section. The locking channel is illuminated with the collimated CW at 1064 nm, while the double-edge channels are illuminated using Rayleigh backscattering from a piece of multimode UV fiber [5]. Here, the Rayleigh backscattering is caused by microscopic refractive index fluctuations along the length of a fiber due to its inherent imperfections. Usually, the inhomogeneities are frozen in the material structure, thus neither Doppler shift nor spectrum broadening occurs in the Rayleigh backscattering along the fiber. In fact, optical time-domain reflectrometry based on Rayleigh scattering has been widely used to detect fault/ imperfection location in fiber optic communications [33].

#167584 - $15.00 USD Received 27 Apr 2012; revised 27 May 2012; accepted 30 May 2012; published 22 Jun 2012

The locking channel has a FWHM of 230 MHz in contrast to the previous value of 1.7GHz as shown in Fig. 1, providing a higher locking accuracy. The frequency shifts among different channels are determined by the height of the fused silica steps deposited on one of the FPI plates. The three channels are synchronized in the frequency domain in this configuration, which allows accurate frequency locking of the laser to the FPI. However, there is still a crucial problem in this method. The frequency offset between the power laser and the seed laser varies from time to time, especially when the laser is reinitiated. Taking this problem into account, the frequency offsets are recorded in the calibration procedure and during the integration time of each LOS wind measurement. Then the difference of the frequency offsets in two cases is calculated and transferred into a systematic error, which is subtracted from each LOS wind profile.

The computer interface installed in the FPI has 16-bit operation and each digital step is 82 pm, which defines an ideal locking accuracy of 185 kHz. To evaluate the accuracy of the frequency locking method, the transmission of the seed laser on the locking channel of the FPI is measured and converted into relative frequency, when the seed laser is exposed to ambient just before a fan. The frequency of 532 nm pulse against the iodine cell is monitored and averaged over every minute. The result is shown in Fig. 4(b). A residual frequency drift within $\pm$ 2.6 MHz is detected. This is due to the slow feedback procedure of the fiber seed laser, which takes about 8 minutes to reach equilibrium after changing the temperature of heaters attached to FBGs. To evaluate the locking accuracy between the FPI and the seed laser, the FPI is scanned until the seed laser is aligned to the half-maximum position on the right locking slope. Then, the close-loop locking procedure controls the cavity length of the FPI to guarantee the alignment of the FPI and the seed laser. The transmission value of the seed laser on the locking channel is measured and averaged every minute, and then transformed into the relative frequency based on the locking curve characterized in the calibration procedure. Despite of the frequency drift of the seed laser, a locking accuracy of $\pm$ 0.3 MHz is realized, as shown in Fig. 4(c). Take advantage of the cavity-tunable FPI, we need not control the absolute frequency of the seed laser as accurate as in the ALADIN system. The absolute frequency control loop used in the transmitter is to avoid monotonic frequency drift of the seed laser, since the cavity tune range of the FPI is limited to 3.5 μm (corresponding to 236.6 GHz at 355 nm).

To reduce the ambient influence, several updates are made to the mobile lidar. All optical systems are separated from the laser power supply and cooling water system. The seed laser is enclosed in a temperature-regulated chamber with temperature stability better than $\pm 0.1℃$ to stabilize the outgoing frequency of the seed laser. The temperature fluctuation of the cooling water to the laser heads is strictly stabilized within $\pm 0.2℃$ to stabilize the cavity length of the low power oscillator, and to maintain a small and constant divergence of the laser beam [21]. The power laser and optical receiver are mounted on a vibration-isolated optical table, providing transmissibility of 0.3% at vibration frequency of 30 Hz. The receiver is pressure sealed and temperature controlled with $\pm 0.1℃$ stability to prevent condensation forming on the FPI mirrors, and to minimize distortions of the mirror surfaces due to temperature gradients in the glass. The temperature of the iodine cell is controlled with a stability of $\pm 0.2℃$ to reduce the frequency drift corresponding to the Doppler broadening [21, 22].

4. Wind observations

Wind observation is carried out in the Taklamakan desert ($42.1°N$, $87.1°E$) in northwest of China, throughout September and October, 2011. Figure 5 shows the mobile Rayleigh Doppler lidar and the support vehicle behind it. The whole lidar system is integrated on the first truck. Considering stability of the mobile lidar, power generators and a mobile office is mounted on the support vehicle.

#167584 - $15.00 USD Received 27 Apr 2012; revised 27 May 2012; accepted 30 May 2012; published 22 Jun 2012

Fig. 5. The USTC Rayleigh Doppler lidar in experiment

For the convenience of deriving analytical equations of the double-edge technique, the lidar backscattering from atmospheric molecules is approximated to have a Gaussian-shaped Rayleigh spectrum. Actually, the line shape is changed by Brillouin doublet, resulting from light scattering on spontaneous acoustic waves propagating in the atmosphere. The superimposed "Rayleigh-Brillouin" spectrum is rigorously called the "Cabannes" line [34]. Considering the impact of temperature and pressure, the Tenti S6 model is used to calculate the Cabannes line at different altitude in the wind-retrieval algorithm [35]. In this work, the temperature profile is obtained from ECMWF (European Center for Medium range Weather Forecast) analysis, when radiosonde data are not available.

The number of photons N_1 and N_2 after the two edge channels are detected using photon counting PMTs, providing high sensitivity in the upper troposphere and stratosphere, where the backscattered signals are low. Due to the dynamic range limitation of the PMTs, the wind observation altitude is gated from 8 to 40 km. In this work, the so-called Rayleigh response function is defined as

$$R(\upsilon_D) = \left[N_1(\upsilon_D) - N_2(\upsilon_D)\right] / \left[N_1(\upsilon_D) + N_2(\upsilon_D)\right]. \tag{1}$$

Where, υ_D is the Doppler frequency shift, and the photon number is given by

$$N_i(\upsilon_D) = a_i \int_{-\infty}^{+\infty} T_i(\upsilon) I(\upsilon - \upsilon_D) d\upsilon, \tag{2}$$

where, $i = (1,2)$ stands for left channel and right channel of the FPI, respectively. a_i is a calibration constant. $T_i(\upsilon)$ is the transmission curve characterized in the calibration procedure, as shown in Fig. 4(a). $I(\upsilon)$ is the power spectrum of the backscattered signal. Thanks to the UV working wavelength of our system, the impact of Mie contamination in the altitude range from the upper troposphere to the stratosphere is neglected in this work [35]. Thus $I(\upsilon)$ is computed using Tenti S6 model at different temperature and pressure in the inversion process. To avoid time-consuming computation of the convolution product Eq. (2) and the Tenti S6 model, a look-up-table of Rayleigh response is computed and stored after transmission curves are characterized. In the data processing procedure, we fit the measured transmission curves of the FPI to a new developed mathematical model

$$\begin{aligned} T(\upsilon) = B + T_p \left\{ 1 + 2\sum_{n=1}^{M} R_e^n \cos\left[\frac{2\pi n(\upsilon - \upsilon_c)}{\upsilon_{FSR}} \frac{1+\cos\theta_0}{2} \right] \cdot \sin c\left(\frac{2n\upsilon_0}{\upsilon_{FSR}} \frac{1-\cos\theta_0}{2} \right) \right. \\ \left. \cdot \exp\left[-\left(\frac{\pi n \Delta\upsilon_L}{\upsilon_{FSR}} \frac{1+\cos\theta_0}{2} \right)^2 \right] \right\} \end{aligned} \tag{3}$$

#167584 - $15.00 USD Received 27 Apr 2012; revised 27 May 2012; accepted 30 May 2012; published 22 Jun 2012

Where, B is the background constant, T_p is the peak value of the transmission curve, R_e is the effective reflectivity, v_{FSR} is the FSR of the FPI, $\Delta\upsilon_L$ is the half-width of the laser pulse at $1/e$ intensity, $\theta_0 = 1.25$ mrad is the half-maximum divergence of the collimated beams to the FPI, υ_0 is the optical frequency of the UV pulse, υ_c is the center frequency of the transmission curve, $M = 30$ is a empirical number used in the nonlinear least squares fit procedure. Equation (3) is a periodic function used to describe the FPI transmission curves instead of the single-peak Voigt function [5]. A detailed development of this numerical model is beyond the scope of this paper and will be introduced somewhere else. Finally the inversion of Doppler shift υ_D with a measured response value $R_m(\upsilon_D)$ is performed by interpolation. Once the Doppler shift is retrieved, the LOS wind velocity is calculated as

$$V_{LOS} = \upsilon_D \lambda / 2. \tag{4}$$

In the experiment, the lidar works in a step stare scanning mode, which means the scanner points at a fixed zenith angle of 30° along each of the four cardinal directions clockwisely, i.e., the azimuth angle sequence is 0° (north), 90°, 180° and 270°. The four LOS wind profiles are combined to derive the wind velocity and direction by assuming that the wind field is homogeneous horizontally.

An example of typical raw data in the experiment is shown in Fig. 6(a). In this system, the statistical standard error of wind measurement is suppressed by using a long integration time of half an hour for each LOS pointing, and the available height resolution is sacrificed from 100 m (below 20 km) to 500 m (above 20 km), as shown in Fig. 6(b). The statistical standard error of wind measurements can be estimated, assuming the photon noises of the photon counting PMTs are uncorrelated and follow Possion statics with SNR inversely proportional to the square root of photon counts on each detector [25]. Temporally, there is no interferometric filter with optical narrowband in the receiver, making the lidar operates at night only. Judging from the raw signal in the altitude range from 70 km to 80 km in Fig. 6, one can see that the dark counts of the PMTs and background noise is negligible.

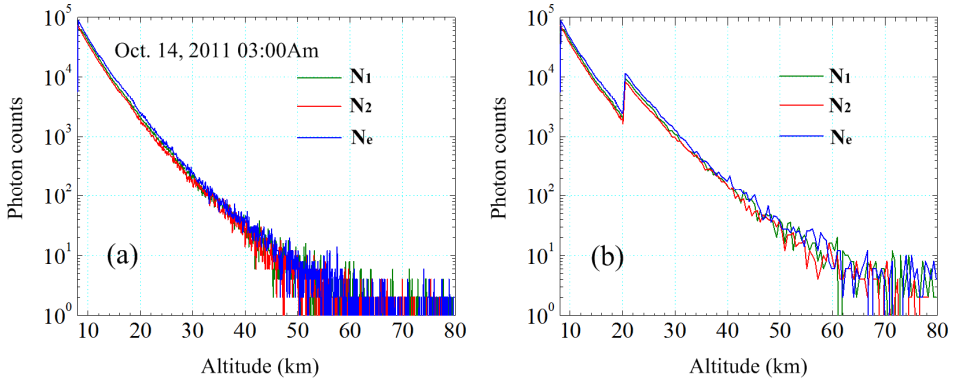

Fig. 6. Profiles of backscattered signals on the two edge channels (N_1, N_2) and on the energy monitoring channel (N_e). The height resolution is changed from 100 m (a) to 500 m (b) above 20 km.

To validate the performance of the Rayleigh Doppler lidar, comparison of wind measurements from the lidar, radiosonde and the ECMWF analysis is made in every morning from September to October, if weather condition permits lidar operation. Two typical experiment results are shown in Fig. 7. Wind measured by Rayleigh Doppler lidar is plotted with error bars, including the calibration uncertainty, model temperature deviation (assumed to be ± 5 K [25]) and statistical standard error.

#167584 - $15.00 USD Received 27 Apr 2012; revised 27 May 2012; accepted 30 May 2012; published 22 Jun 2012

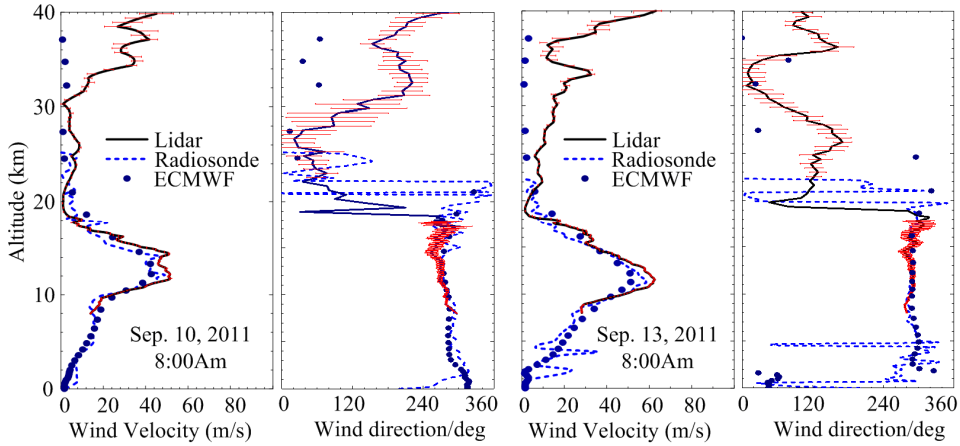

Fig. 7. Profiles of wind speed and direction measured by the Rayleigh Doppler lidar (solid line) compared with data measured by radiosonde (dashed line) and data from ECMWF (filled circle). In the altitude range where wind velocity is below the measurement error, wind direction from the lidar has no meaning, and its error bars are not plotted.

In the altitude of 12.6 km, clear evidence of mid-altitude jet with maximum speed of 51 m/s and 63 m/s is observed at 8:00 (Beijing time, corresponding to 0:00 UT) on the morning of Sep. 10 and Sep. 13, 2011. Wind profiles from different techniques show good agreement below 25 km. At altitude above 25 km where radiosonde data is not available, large difference between the ECMWF and the Rayleigh Doppler lidar is observed for this case, and similar phenomena have been reported recently by ALOMAR [21]. It is noteworthy that, wind observations taken from an airborne Doppler wind lidar reduced the error significantly in analyses and forecasts of the ECMWF system for tropospheric winds [36, 37].

Before a further comparison between the lidar and radiosonde, structure of the atmosphere under the altitude of 25 km is analyzed using temperature profiles obtained by radiosondes. Starting at the earth's surface, the temperature decreases up to a layer known as the tropopause, which separates the troposphere from the stratosphere. It is defined by the World Meteorological Organization (WMO) as the lowest level at which the lapse rate decreases to 2 $K\text{km}^{-1}$ or less, provided that the average lapse rate between the level and all higher levels within 2 km does not exceed 2 $K\text{km}^{-1}$ [38]. The altitude of the tropopause is shown in Fig. 8. In the transition region, the temperature lapse rate changes abruptly over the two months.

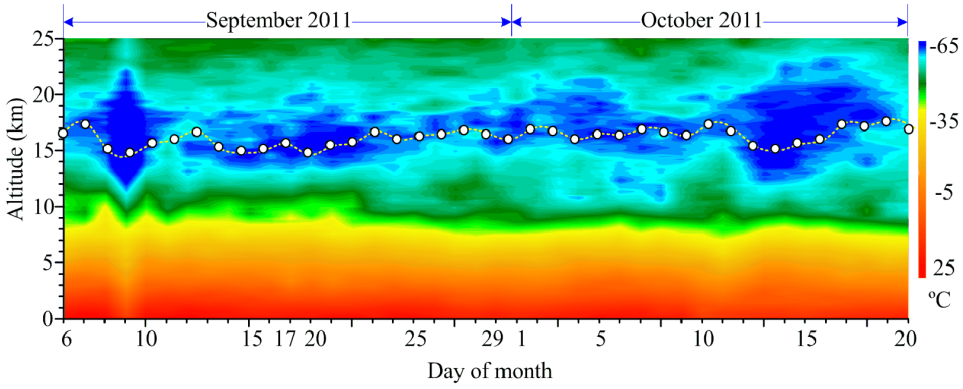

Fig. 8. Time-altitude plot of temperature detected using radiosonde. The tropopause is shown (dashed line with circles).

#167584 - $15.00 USD Received 27 Apr 2012; revised 27 May 2012; accepted 30 May 2012; published 22 Jun 2012

To evaluate the accuracy of the Rayleigh Doppler lidar, wind data from the lidar and radiosonde at 8:00 are analyzed statistically. The histograms presented in Fig. 9 summarize the wind difference in the altitude range from 8 km to 20 km for 28 days. Specifically, Fig. 9(a) and Fig. 9(b) are histogram distributions of velocity difference and direction difference from 8 km to tropopause, and Fig. 9 (c) and Fig. 9(d) are histogram distributions of velocity difference and direction difference from tropopause to 20 km. The mean differences of velocity and direction are −1.1 m/s and 2.3°below the tropopause, and −1.4 m/s and 1.5°above the tropopause. The standard deviations of velocity and direction are 3.9 m/s and 16.9°under the tropopause, and 5.1 m/s and 23.6°above the tropopause. In this experiment, the velocity uncertainty and direction uncertainty of the homemade GPS radiosonde (CASIC, CF-06-A) are 0.2 m/s and 2°, when wind speed is above 3 m/s. The hydrogen balloon takes off from a site 12 km away from the lidar, and it takes 2 hours for the radiosonde to ascend to an altitude of 20 km. Given the photon counts of the atmospheric backscattering at 10 km, the velocity measurement uncertainty ($\pm 1\sigma$) of the lidar can be estimated to be about 1.6 m/s. Obviously, the mean difference and standard deviation are larger than estimated values, which may be mainly due to two reasons. Firstly, the wind-retrieval algorithm assumes a horizontal homogeneity of the wind field. Secondly, the radiosonde measures wind via its ascending process instantaneously, while the lidar makes time-averaged wind measurement over a volume.

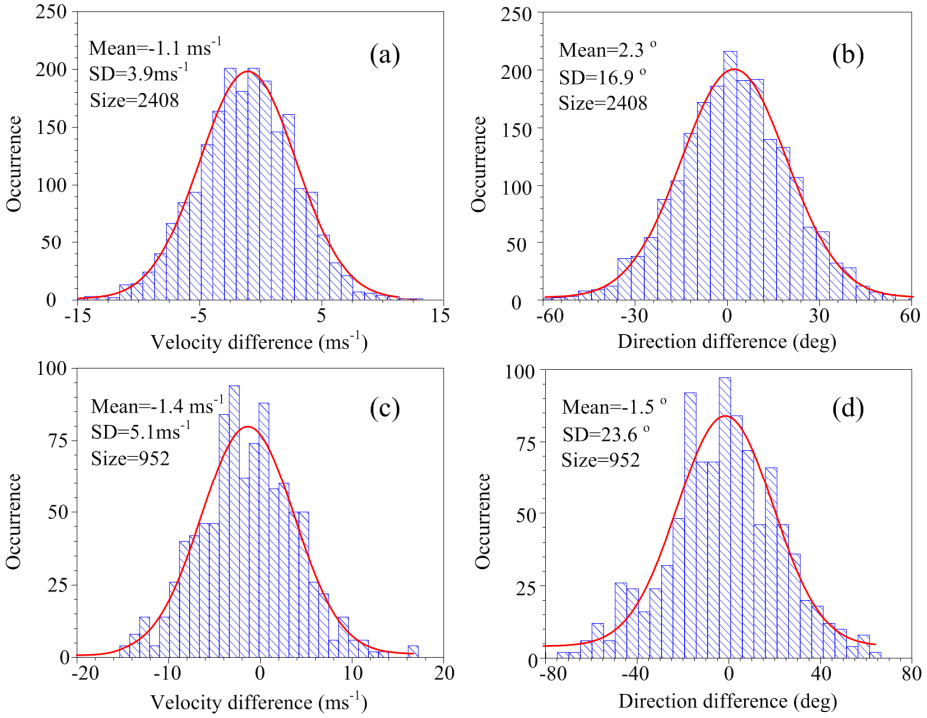

Fig. 9. Statistics of the difference in wind measurements between the lidar and radiosonde (red lines are the Gaussian fit results to the data): (a) and (b) are histogram distributions of velocity difference and direction difference from 8 km to tropopause, (c) and (d) are histogram distributions of velocity difference and direction difference from tropopause to 20 km.

Continuous wind field observation is performed every night throughout September and October, 2011, as shown in Fig. 10. Experiment data with velocity error larger than 10 m/s are not plotted. Due to the weather condition and desert dust, semi-continuous wind field of 34 nights were observed. Despite of this limitation, the dynamic structure of the mid-attitude atmosphere and its evolution are clearly shown in Fig. 8. The high-altitude tropospheric jet at

#167584 - $15.00 USD Received 27 Apr 2012; revised 27 May 2012; accepted 30 May 2012; published 22 Jun 2012

12 km is very strong in September and fades out in October generally. Another interesting phenomenon is the stable quasi-zero wind layer centered at 20 km with a thickness of about 4 km. In the meantime, the wind direction changes from west (from 8 to 20 km) to east (above 20 km) obviously, from Sep. 6 to Oct. 10. After that, the wind direction of the high-altitude tropospheric jet turned from west to east with its fading in velocity, at some nights in the middle of October. It should be noted that, wind velocity observed in the altitude range from 24 km to 40 km using lidar is larger than the ECMWF results. This remaining difference and the oscillation of the wind velocity will be investigated for gravity wave studies in the near future.

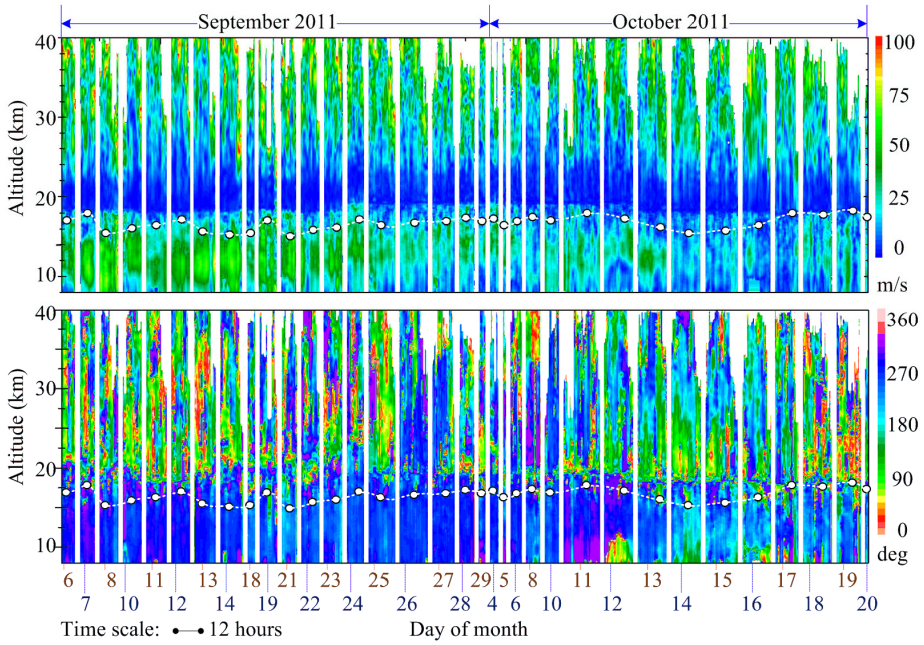

Fig. 10. Time-altitude plot of semi-continuous observation of mid-altitude wind field in September and October, 2011. Local midnights are tagged. Time scale is plotted in the lower left corner. The altitude of the tropopause is shown (dashed line with circles) for reference. The data with velocity error larger than 10 m/s are not plotted. The wind direction in the quasi-zero wind layer has no meaning, since the error of velocity measurement is larger than the wind velocity. The minimum velocity error and the minimum direction error in this experiment are estimated to be 0.86 m/s and $3.6°$, respectively.

5. Conclusion and future research

A mobile Rayleigh Doppler lidar was successfully updated to perform direct detection of middle-atmospheric wind from 8 km to 40 km. A system-level optical frequency control method was integrated into the system for automatic operation and performance enhancement. In the comparison experiments, wind measurements from the lidar, radiosonde and the ECMWF analysis were in good agreement in the altitude range from 8 km to 25km. Continuous measurement of mid-altitude wind field was performed. Some dynamic atmospheric phenomena were observed.

For future research, a narrow band interferometer filter should be added in the receiver to extend the capability for daytime observations. Temporally, changes in parallelism and cavity length of the FPI are detected by a three-axis capacitance bridge stabilization system, which leads to thermal instability. Recently, we demonstrated a novel femtosecond ranging technique [39, 40], which will be introduced to measure the absolute cavity length and control parallelism of the FPI. To study the dynamic process in the altitude range from 10 km to 60

#167584 - $15.00 USD Received 27 Apr 2012; revised 27 May 2012; accepted 30 May 2012; published 22 Jun 2012

km, three independent mobile Rayleigh Doppler lidars with telescope diameters of 1 meter are under construction. Meteorological rocket sondes based on GPS will be used to validate the lidar performance in the near future.

Acknowledgments

The European Centre for Medium-Range Weather Forecasts (ECMWF) is gratefully acknowledged for providing the wind and temperature data. The authors are grateful to the editors and two anonymous reviewers for their constructive comments. This work was supported by the Chinese Academy of Sciences (KZZD-EW-01-1) and National Natural Science Foundation of China (41174130 and 41174131).

#167584 - $15.00 USD Received 27 Apr 2012; revised 27 May 2012; accepted 30 May 2012; published 22 Jun 2012